The Entire Landslide Velocity

1 author:

Shiva P. Pudasaini
University of Bonn
131 PUBLICATIONS   **3,839** CITATIONS

SEE PROFILE

Some of the authors of this publication are also working on these related projects:

Debris-flow generated impulse waves View project

A novel and unified solution to multi-phase mass flows: U_MultiSol View project

The Entire Landslide Velocity

Shiva P. Pudasaini

Technical University of Munich, School of Engineering and Design
Chair of Landslide Research
Arcisstrasse 21, D-80333, Munich, Germany
E-mail: shiva.pudasaini@tum.de

Abstract: The enormous destructive energy carried by a landslide is principally determined by its velocity. Pudasaini and Krautblatter (2022) presented a simple, physics-based analytical landslide velocity model that simultaneously incorporates the internal deformation and externally applied forces. They also constructed various general exact solutions for the landslide velocity. However, previous solutions are incomplete as they only apply to accelerating motions. Here, I advance further by constructing several new general analytical solutions for decelerating motions and unify these with the existing solutions for the landslide velocity. This provides the complete and honest picture of the landslide in multiple segments with accelerating and decelerating movements covering its release, motion through the track, the run-out as well as deposition. My analytical procedure connects several accelerating and decelerating segments by a junction with a kink to construct a multi-sectoral unified velocity solution down the entire path. Analytical solutions reveal essentially different novel mechanisms and processes of acceleration, deceleration and the mass halting. I show that there are fundamental differences between the landslide release, acceleration, deceleration and deposition in space and time as the dramatic transition takes place while the motion changes from the driving force dominated to resisting force dominated sector. I uniquely determine the landslide position and time as it switches from accelerating to decelerating state. Considering all the accelerating and decelerating motions, I analytically obtain the exact total travel time and the travel distance for the whole motion. Different initial landslide velocities with ascending or descending fronts result in strikingly contrasting travel distances, and elongated or contracted deposition lengths. Time and space evolution of the marching landslide with initial velocity distribution consisting of multiple peaks and troughs of variable strengths and extents lead to a spectacular propagation pattern with different stretchings and contractings resulting in multiple waves, foldings, crests and settlements. The analytical method manifests that, computationally costly numerical solutions may now be replaced by a highly cost-effective, unified and complete analytical solution down the entire track. This offers a great technical advantage for the geomorphologists, landslide practitioners and engineers as it provides immediate and very simple solution to the complex landslide motion.

1 Introduction

The dynamics of a landslide are primarily controlled by its velocity which plays a key role for the assessment of landslide hazards, design of protective structures, mitigation measures and landuse planning (Johannesson et al., 2009; Faug, 2010; Dowling and Santi, 2014). Thus, a proper and full understanding of landslide velocity is a crucial requirement for an appropriate modelling of landslide impact force because the associated hazard is directly related to the landslide velocity (Evans et al., 2009; Dietrich and Krautblatter, 2019). However, the mechanical controls of the evolving velocity, runout and impact energy of the landslide have not yet been fully understood.

On the one hand, the available data on landslide dynamics are insufficient while on the other hand, the proper understanding and interpretation of the data obtained from field measurements are often challenging. This is because of the very limited information of the boundary conditions and the material properties. Moreover, dynamic field data are rare and after event static data are often only available for single locations (de Haas et al., 2020). So, much of the low resolution measurements are locally or discretely based on points in time and space (Berger et al., 2011; Theule et al., 2015; Dietrich and Krautblatter, 2019). This is the reason for why laboratory or field experiments (Iverson and Ouyang, 2015; de Haas and van Woerkom, 2016; Pilvar et

Earth **Surface**
Dynamics
Discussions

EGU

⁴⁶ al., 2019; Baselt et al., 2021) and theoretical modelling (Le and Pitman, 2009; Pudasaini, 2012; Pudasaini and
⁴⁷ Mergili, 2019) remain the major solutions of the problems associated with the mass flow dynamics. Several
⁴⁸ comprehensive numerical modelling for mass transports are available (McDougall and Hungr, 2005; Frank et
⁴⁹ al., 2015; Iverson and Ouyang, 2015; Cuomo et al., 2016; Mergili et al., 2020; Liu et al. 2021). Yet, numer-
⁵⁰ ical simulations are approximations of the physical-mathematical model equations and their validity is often
⁵¹ evaluated empirically (Mergili et al., 2020). In contrast, exact, analytical solutions can provide better insights
⁵² into complex flow behaviors (Faug et al., 2010; Gauer, 2018; Pudasaini and Krautblatter, 2021,2022; Faraoni,
⁵³ 2022). Furthermore, analytical and exact solutions to non-linear model equations are necessary to elevate the
⁵⁴ accuracy of numerical solution methods based on complex numerical schemes (Chalfen and Niemiec, 1986;
⁵⁵ Pudasaini, 2016). This is very useful to interpret complicated simulations and/or avoid mistakes associated
⁵⁶ with numerical simulations. However, the numerical solutions (Mergili et al., 2020; Shugar et al., 2021) can
⁵⁷ cover the broad spectrum of complex flow dynamics described by advanced mass flow models (Pudasaini and
⁵⁸ Mergili, 2019), and once tested and validated against the analytical solutions, may provide even more accurate
⁵⁹ results than the simplified analytical solutions (Pudasaini and Krautblatter, 2022).

⁶⁰ Since Voellmy's pioneering work, several analytical models and their solutions have been presented for mass
⁶¹ movements including landslides, avalanches and debris flows (Voellmy, 1955; Salm, 1966; Perla et al., 1980;
⁶² McClung, 1983). However, on the one hand, all of these solutions are effectively simplified to the mass point
⁶³ or center of mass motion. None of the existing analytical velocity models consider advection or internal defor-
⁶⁴ mation. On the other hand, the parameters involved in those models only represent restricted physics of the
⁶⁵ landslide material and motion. Pudasaini and Krautblatter (2022) overcame those deficiencies by introducing a
⁶⁶ simple, physics-based general analytical landslide velocity model that simultaneously incorporates the internal
⁶⁷ deformation and externally applied forces, consisting of the net driving force and the viscous resistant. They
⁶⁸ showed that the non-linear advection and external forcing fundamentally regulate the state of motion and
⁶⁹ deformation. Since analytical solutions provide the fastest, the most cost-effective and best rigorous answer
⁷⁰ to the problem, they constructed several general exact analytical solutions. Those solutions cover the wider
⁷¹ spectrum of landslide velocity and directly reduce to the mass point motion as their solutions bridge the gap
⁷² between the negligibly deforming and geometrically massively deforming landslides. They revealed the fact
⁷³ that shifting, up-lifting and stretching of the velocity field stem from the forcing and non-linear advection. The
⁷⁴ intrinsic mechanism of their solution described the breaking wave and emergence of landslide folding. This
⁷⁵ demonstrated that landslide dynamics are architectured by advection and reigned by the system forcing.

⁷⁶ However, the landslide velocity solutions presented by Pudasaini and Krautblatter (2022) are only applicable
⁷⁷ for the accelerating motions associated with the positive net driving forces, and thus are incomplete. Here, I
⁷⁸ extend their solutions that cover the entire range of motion, from initiation to acceleration, to deceleration to
⁷⁹ deposition as the landslide mass comes to a halt. This includes both the motions with positive and negative
⁸⁰ net driving forces. This constitutes a unified foundation of landslide velocity in solving technical problems.
⁸¹ As exact, analytical solutions disclose many new and essential physics of the landslide release, acceleration,
⁸² deceleration and deposition processes, the solutions derived in this paper may find applications in geomorpho-
⁸³ logical, environmental, engineering and industrial mass transports down entire slopes and channels in quickly
⁸⁴ and adequately describing the entire flow dynamics, including the flow regime changes.

⁸⁵ 2   The Model

⁸⁶ For simplicity, I consider a geometrically two-dimensional motion down a slope. Let t be time, (x, z) be the
⁸⁷ coordinates and (g^x, g^z) the gravity accelerations along and perpendicular to the slope, respectively. Let, h
⁸⁸ and u be the flow depth and the mean flow velocity of the landslide along the slope. Similarly, γ, α_s, μ be
⁸⁹ the density ratio between the fluid and the solid particles ($\gamma = \rho_f / \rho_s$), volume fraction of the solid particles
⁹⁰ (coarse and fine solid particles), and the basal friction coefficient ($\mu = \tan \delta$), where δ is the basal friction angle
⁹¹ of the solid particles, in the mixture material. Furthermore, K is the earth pressure coefficient (Pudasaini and
⁹² Hutter, 2007), and β is the viscous drag coefficient. By reducing the multi-phase mass flow model (Pudasaini

and Mergili, 2019), Pudasaini and Krautblatter (2022) constructed the simple landslide velocity equation:

$$\frac{\partial u}{\partial t} + u\frac{\partial u}{\partial x} = \alpha^a - \beta u^2, \tag{1}$$

where α^a and β constitute the net driving and the resisting forces in the system. Moreover, α^a is given by the expression $\alpha^a := g^x - (1-\gamma)\alpha_s g^z \mu - g^z \{((1-\gamma) K + \gamma) \alpha_s + (1 - \alpha_s)\} h_g$ (this includes the forces due to gravity, Coulomb friction, lubrication, and liquefaction as well as the surface gradient indicated by h_g), and β is the viscous drag coefficient.

Pudasaini and Krautblatter (2022) constructed many exact analytical solutions to the landslide velocity equation (1). However, their solutions were restricted to the physical situation in which the net driving force is positive, i.e., $\alpha^a > 0$. Following the classical method by Voellmy (Voellmy, 1955) and extensions by Salm (1966) and McClung (1983), the velocity model (1) can be amended and used for multiple slope segments to describe the accelerating and decelerating motions as well as the landslide run-out. These are also called the release, track and run-out segments of the landslide, or avalanche (Gubler, 1989). However, for the gentle slope, or the run-out, the frictional force may dominate gravity. In this situation, the sign of α^a in (1) changes. So, to complement the solutions constructed in Pudasaini and Krautblatter (2022), here, I consider (1) with negative net driving force resulting in the decelerating motion, and finally the landslide deposition. For this, I change the sign of α^a and rewrite (1) as:

$$\frac{\partial u}{\partial t} + u\frac{\partial u}{\partial x} = -\alpha_d - \beta u^2. \tag{2}$$

Note that ^{a} and $_d$ in α^a and α_d in (1) and (2) indicate the accelerating (ascending) and decelerating (descending) motions, respectively. We follow these notations for all the models and solutions considered and developed below.

The main purpose here is to construct several new analytical solutions to (2), and combine these with the existing solutions (Pudasaini and Krautblatter, 2022) for (1). This facilitates the description of the landslide motion down a slope consisting of multiple segments with accelerating and decelerating movements, with positive and negative net driving forces, as well as the landslide run-out. This will provide us with the complete and unified picture of the landslide motions in different segments- from release to track to run-out and deposition as required by the practitioners.

Terminology and convention: To avoid any possible ambiguity, I define the terminology for accelerating and decelerating motions and motions with ascending and descending velocities. Consider model (1). Then, we have the following two situations.

Accelerating motion − I: The landslide accelerates if the total system force $\alpha^a - \beta u^2 > 0$. This happens only if $\alpha^a > 0$, that is, when the net driving force is positive, and the initial velocity u_0 satisfies the condition $u_0 < \sqrt{\alpha^a/\beta}$.

Decelerating motion − II: The landslide decelerates if $\alpha^a - \beta u^2 < 0$. This can happen in two completely different situations.

II.1 − Weak-deceleration: First, consider $\alpha^a > 0$, but relatively high initial velocity such that $u_0 > \sqrt{\alpha^a/\beta}$. Then, although the net driving force is positive, due to the high value of the initial velocity than the characteristic limit velocity of the system $\sqrt{\alpha^a/\beta}$, the landslide attains decelerating motions due to the high drag force, and approaches down to $\sqrt{\alpha^a/\beta}$ as the landslide moves. I call this the weak-deceleration.

II.2 − Strong-deceleration: Second, consider $\alpha^a = -\alpha_d < 0$, which is the state of the negative net driving force associated with the system (2). Then, for any choice of the initial velocity, the landslide must decelerate. I call this the strong-deceleration. The decelerating velocity in **II.2** is always below the decelerating velocity in **II.1**

Ascending and descending motions: Unless otherwise stated and without loss of generality, I make the following convention. When the net driving force is positive and **I** is satisfied, the accelerating landslide motion

135 (velocity) is also called the ascending motion. Because, in this situation, the motion is associated with the
136 ascending velocity. When the net driving force is negative or **II.2** is satisfied, the decelerating landslide motion
137 (velocity) is also called the descending motion, because for this, the velocity always decreases. I will separately
138 treat **II.1** in Section 5.4.

139 The landslide velocity solutions for **I** and **II.1** are associated with the positive net driving forces, and have
140 been presented in Pudasaini and Krautblatter (2022). Here, I present solutions for **II.2** associated with the
141 negative net driving force and unify them with previous solutions. This completes the construction of simple
142 analytical solutions.

3 The Entire Landslide Velocity: Simple Solutions

144 As (2) describes fundamentally different process of landslide motion than (1), for the model (2), all solutions
145 derived by Pudasaini and Krautblatter (2022) must be thoroughly re-visited with the initial condition for veloc-
146 ity of the following segment being that obtained from the lower end of the upstream segment. This way, we can
147 combine solutions to models (1) and (2) to analytically describe the landslide motion for the entire slope, from
148 its release, through the track to the run-out, including the total travel distance and the travel time. This is the
149 novel aspect of this contribution which makes the present solution system complete that the practitioners and
150 engineers can directly apply these solutions to solve their technical problems. However, note that, decelerating
151 motion can be constructed independent of whether or not it follows an accelerating motion. In other situation,
152 accelerating motion could follow the decelerating motion. So, depending on the state of the net driving forces,
153 different scenarios are possible.

154 Because of their increasing and decreasing behaviors, velocity solutions associated with the model (1) is indi-
155 cated by the symbol $\nearrow$, and that associated with the model (2) it is indicated by the symbol $\searrow$. These are
156 the ascending and descending motions, respectively. All the solutions indicated by the symbol $\searrow$ are entirely
157 new. By combining these two types of solutions, we obtain the complete solution for the landslide motion, i.e.,
158 'the solution $\nearrow$ + the solution $\searrow$ = the complete solution'.

3.1 Steady-state motion

160 The steady-state solution describes one of the simplest states of dynamics that are independent of time ($\partial u/\partial t =$
161 0). So, I begin with constructing simple analytical solutions for the steady-state landslide velocity equations,
162 reduced from (1) and (2):

$$u\frac{\partial u}{\partial x} = \alpha^a - \beta u^2, \tag{3}$$

163 and

$$u\frac{\partial u}{\partial x} = -\alpha_d - \beta u^2, \tag{4}$$

164 respectively. Following Pudasaini and Krautblatter (2022), the steady-state solution for (3) takes the form:

$$\nearrow u(x; \alpha^a, \beta) = \sqrt{\frac{\alpha^a}{\beta}\left[1 - \left(1 - \frac{\beta}{\alpha^a}u_0^2\right)\frac{1}{\exp(2\beta(x - x_0))}\right]}, \tag{5}$$

165 where, $u_0 = u(x_0)$ is the initial velocity at x_0. Similarly, the steady-state solution for (4) can be constructed,
166 which reads:

$$\searrow u(x; \alpha_d, \beta) = \sqrt{\frac{1}{\beta}\left[\exp\{-2\beta(x - x_0)\}\left(\beta u_0^2 + \alpha_d\right) - \alpha_d\right]}, \tag{6}$$

167 However, solutions (5) and (6) appear to be structurally similar, and by changing α^a to $-\alpha_d$, (5) can be
168 simplified to yield (6). These solutions describe the dynamics of a landslide (the velocity u) as a function of
169 the downslope position, x, one of the basic dynamic quantities required by engineers and practitioners for the
170 quick assessment of landslide hazards.

3.2 Mass point motion

Assume no or negligible local deformation (e.g., $\partial u/\partial x \approx 0$), or a Lagrangian description. Both are equivalent to the mass point motion. In this situation, only the ordinary differentiation with respect to time is involved, and $\partial u/\partial t$ can be replaced by du/dt. Then, the models (1) and (2) reduce to

$$\frac{du}{dt} = \alpha^a - \beta u^2, \tag{7}$$

and

$$\frac{du}{dt} = -\alpha_d - \beta u^2, \tag{8}$$

respectively, for the positive and negative net driving forces. Solutions to mass point motions provide us with quick information of the landslide motion in time. Such solutions are often required and helpful to analyze the time evolution of primarily largely intact sliding mass without any substantial spatial deformation. So, we proceed with the solution for the mass point motions.

3.2.1 Accelerating landslide

Exact analytical solution for (7) can be constructed, providing the velocity for the landslide motion in terms of a tangent hyperbolic function (Pudasaini and Krautblatter, 2022):

$$\nearrow u\left(t; \alpha^a, \beta\right) = \sqrt{\frac{\alpha^a}{\beta}} \tanh\left[\sqrt{\alpha^a \beta}\left(t - t_0\right) + \tanh^{-1}\left(\sqrt{\frac{\beta}{\alpha^a}}\, u_0\right)\right], \tag{9}$$

where, $u_0 = u(t_0)$ is the initial velocity at time $t = t_0$. The mass point solutions also enable us to exactly obtain the travel time, travel position and distance of the landslide down the slope that I derive below. These quantities are of direct practical importance.

Travel time for accelerating landslide: The travel time for the accelerating landslide in any sector of the flow path can be obtained by using the (maximum) velocity at the right end in that sector, say u_{max}, in (9)

$$\nearrow t_{max} = t_0 + \frac{1}{\sqrt{\alpha^a \beta}}\left[\tanh^{-1}\left(\sqrt{\frac{\beta}{\alpha^a}} u_{max}\right) - \tanh^{-1}\left(\sqrt{\frac{\beta}{\alpha^a}} u_0\right)\right]. \tag{10}$$

The position of accelerating landslide: Since $u(t) = dx/dt$, (9) can be integrated to obtain the landslide position as a function of time (Pudasaini and Krautblatter, 2022):

$$\nearrow x\left(t; \alpha^a, \beta\right) = x_0 + \frac{1}{\beta} \ln\left[\cosh\left\{\sqrt{\alpha^a \beta}\left(t - t_0\right) - \tanh^{-1}\left(\sqrt{\frac{\beta}{\alpha^a}} u_0\right)\right\}\right] - \frac{1}{\beta}\ln\left[\cosh\left\{-\tanh^{-1}\left(\sqrt{\frac{\beta}{\alpha^a}} u_0\right)\right\}\right], \tag{11}$$

where $x_0 = x(t_0)$ corresponds to the position at the initial time t_0.

The travel distance for accelerating landslide: The maximum travel distance x_{max} is achieved by setting $t = t_{max}$ from (10) in to (11), yielding:

$$\nearrow x_{max} = x_0 + \frac{1}{\beta}\ln\left[\cosh\left\{\sqrt{\alpha^a \beta}\left(t_{max} - t_0\right) - \tanh^{-1}\left(\sqrt{\frac{\beta}{\alpha^a}} u_0\right)\right\}\right] - \frac{1}{\beta}\ln\left[\cosh\left\{-\tanh^{-1}\left(\sqrt{\frac{\beta}{\alpha^a}} u_0\right)\right\}\right]. \tag{12}$$

Solutions (9)-(12) provide us the velocity of the negligibly deformable (or non-deformable) accelerating landslide together with its travel time, position and travel distance, supplying us with all necessary information required to fully describe the state of the landslide motion.

3.2.2 Decelerating landslide

However, the exact analytical solution for (8), i.e., the velocity of the decelerating landslide, appears to be the negative of a tangent function:

$$\searrow u\left(t;\alpha_d,\beta\right) = -\sqrt{\frac{\alpha_d}{\beta}}\tan\left[\sqrt{\alpha_d\beta}\left(t-t_0\right)+\tan^{-1}\left(-\sqrt{\frac{\beta}{\alpha_d}}u_0\right)\right], \quad (13)$$

where, $u_0 = u\left(t_0\right)$ is the initial velocity at time $t = t_0$. The solution in (13) is fundamentally different than the one in (9) for the accelerating landslide. In contrast to (9), which always have upper ($u > \sqrt{\alpha^a/\beta}$) or lower bound ($u < \sqrt{\alpha^a/\beta}$) (depending on the initial condition), (13) provides only the decreasing (velocity) solution without any lower bound that must be constrained with the possible (final) velocity in the sector under consideration, say, u_f, particularly $u_f = 0$, when the landslide comes to a halt.

Travel time for decelerating landslide: The maximum travel time in the sector under consideration, t_{max}, is achieved from (13) by setting the velocity at the right end of this sector, say, u_{min} i.e.,

$$\searrow t_{max} = t_0 + \frac{1}{\sqrt{\alpha_d\beta}}\left[\tan^{-1}\left(-\sqrt{\frac{\beta}{\alpha_d}}u_{min}\right) - \tan^{-1}\left(-\sqrt{\frac{\beta}{\alpha_d}}u_0\right)\right]. \quad (14)$$

The final time the mass comes to a standstill is obtained from (14) by setting $u_{min} = 0$.

The position of decelerating landslide: Again, by setting the relation $u(t) = dx/dt$, (13) can be integrated to obtain the landslide position as a function of time:

$$\searrow x\left(t;\alpha_d,\beta\right) = x_0 + \frac{1}{\beta}\ln\left[\cos\left\{\tan^{-1}\left(\sqrt{\frac{\beta}{\alpha_d}}u_0\right) - \sqrt{\alpha_d\beta}\left(t-t_0\right)\right\}\right] - \frac{1}{\beta}\ln\left[\cos\left\{\tan^{-1}\left(\sqrt{\frac{\beta}{\alpha_d}}u_0\right)\right\}\right], \quad (15)$$

where $x_0 = x(t_0)$ corresponds to the position at the initial time t_0.

The travel distance for decelerating landslide: The maximum travel distance x_{max} is achieved by setting $t = t_{max}$ from (14) in to (15), yielding:

$$\searrow x_{max} = x_0 + \frac{1}{\beta}\ln\left[\cos\left\{\tan^{-1}\left(\sqrt{\frac{\beta}{\alpha_d}}u_0\right) - \sqrt{\alpha_d\beta}\left(t_{max}-t_0\right)\right\}\right] - \frac{1}{\beta}\ln\left[\cos\left\{\tan^{-1}\left(\sqrt{\frac{\beta}{\alpha_d}}u_0\right)\right\}\right]. \quad (16)$$

Solutions (13)-(16) supply us with the velocity of practically non-deformable decelerating landslide including its travel time, position and travel distance. All these information are necessary to fully characterise the landslide dynamic.

Total time and total travel distance: It is important to note that the overall total time t_{oa} and the overall total travel distance x_{oa} must include all the times in ascending ($\nearrow$) and descending ($\searrow$) motions until the mass comes to the halt, where $_{oa}$ stands for the overall motion. Here, ascending and descending motions refer to the increasing and decreasing landslide velocities in accelerating and decelerating sections of the sliding path.

In this section I constructed simple exact analytical solutions for the accelerating and decelerating landslides when they are governed by simple time-independent (steady-state) or locally non-deformable (mass point) motions. However, their applicabilities are limited due to their respective constraints of not changing in time or no internal deformation.

4 The Entire Landslide Velocity: General Solutions

In reality, the landslide motion can change in time and space. To cope with these situations, we must construct analytical landslide velocity solutions as functions of time and space. Below, I focus on these important aspects. These general solutions cover all the simple solutions presented in the previous section as special cases. The solutions are constructed for both the accelerating and decelerating motions.

4.1 Accelerating landslide − general velocity

Consider the initial value problem for the accelerating landslide motion (1) with the positive net driving force:

$$\frac{\partial u}{\partial t} + u\frac{\partial u}{\partial x} = \alpha^a - \beta u^2, \ \ u(x,0) = s_0(x). \tag{17}$$

This is a non-linear advective−dissipative system, and can be perceived as an inviscid, dissipative, non-homogeneous Burgers' equation (Burgers, 1948). Following the mathematical procedure in Montecinos (2015), Pudasaini and Krautblatter (2022) constructed an exact analytical solution for (17):

$$\nearrow u(x,t) = \sqrt{\frac{\alpha^a}{\beta}} \tanh\left[\sqrt{\alpha^a\beta}\,t + \tanh^{-1}\left\{\sqrt{\frac{\beta}{\alpha^a}}s_0(y)\right\}\right], \tag{18}$$

where $y = y(x,t)$ is given by

$$\nearrow x = y + \frac{1}{\beta}\ln\left[\cosh\left\{\sqrt{\alpha^a\beta}\,t + \tanh^{-1}\left\{\sqrt{\frac{\beta}{\alpha^a}}s_0(y)\right\}\right\}\right] - \frac{1}{\beta}\ln\left[\cosh\left\{\tanh^{-1}\left\{\sqrt{\frac{\beta}{\alpha^a}}s_0(y)\right\}\right\}\right], \tag{19}$$

and, $s_0(x) = u(x,0)$ provides the functional relation for $s_0(y)$. Which is the direct generalization of the mass point solution given by (9).

As in the mass point solutions, (18) and (19) are also primarily expressed in terms of the tangent hyperbolic, and the composite of logarithm, cosine hyperbolic and tangent hyperbolic functions. However, now, these solutions contain important new dynamics embedded into solutions through the terms associated with the function $s_0(y)$ describing the spatial variations in addition to the time variations of landslide dynamics. This makes the general solution system (18) and (19) more complex, but much closer to the reality than simple solutions constructed in Section 3.2.1 that are applicable either for the time or spatial variations of the landslide velocity.

4.2 Decelerating landslide − general velocity

Next, consider the initial value problem for the decelerating landslide motion (2) with the negative net driving force:

$$\frac{\partial u}{\partial t} + u\frac{\partial u}{\partial x} = -\alpha_d - \beta u^2, \ \ u(x,0) = s_0(x). \tag{20}$$

This is also a non-linear advective−dissipative system, or an inviscid, dissipative, non-homogeneous Burgers' equation. Following Pudasaini and Krautblatter (2022) I have constructed an exact analytical solution for (18), which reads:

$$\searrow u(t; \alpha_d, \beta) = -\sqrt{\frac{\alpha_d}{\beta}}\tan\left[\sqrt{\alpha_d\beta}t + \tan^{-1}\left\{-\sqrt{\frac{\beta}{\alpha_d}}s_0(y)\right\}\right], \tag{21}$$

where $y = y(x,t)$ is given by

$$\searrow x(t; \alpha_d, \beta) = y + \frac{1}{\beta}\ln\left[\cos\left\{\tan^{-1}\left\{\sqrt{\frac{\beta}{\alpha_d}}s_0(y)\right\} - \sqrt{\alpha_d\beta}t\right\}\right] - \frac{1}{\beta}\ln\left[\cos\left\{\tan^{-1}\left\{\sqrt{\frac{\beta}{\alpha_d}}s_0(y)\right\}\right\}\right], \tag{22}$$

and, $s_0(x) = u(x,0)$ provides the functional relation for $s_0(y)$. Which is the direct generalization of the mass point solution given by (13).

As in the mass point solutions, (21) and (22) are also basically expressed in terms of the tangent, and the composite of logarithm, cosine and tangent functions. However, these solutions now contain important new dynamics included into the solutions through the terms associated with the function $s_0(y)$ describing the spatial variations in addition to the time variations of landslide dynamics. This makes the general solution system (21) and (22) more complex, but closer to the reality than simple solutions constructed in Section 3.2.2.

General solutions for the landslide velocities evolving as functions of time and position down the entire flow path, from initiation to the propagation, through the track to the run-out and final deposition, are obtained by combining the accelerating solutions (18)-(19) and the decelerating solutions (21)-(22).

Earth **Surface**
Dynamics
Discussions

EGU

5 Results

In order to illustrate the performances of our novel unified exact analytical solutions, below, I present results for different scenarios and physical parameters representing real situations (Pudasaini and Krautblatter, 2022). We can properly choose the slope angle, solid and fluid densities, the solid volume fraction, basal friction angle of the solid, earth pressure coefficient, and the free-surface gradient such that α^a can be as high as 7, α_d can be as high as 2, and β can be between 0.01 and 0.0025. In what follows, without loss of generality, the parameter values for α^a, α_d and β are chosen from these domains. However, other values of these physical and model parameters are possible within their admissible domains.

Landslide deceleration begins as the resisting forces overtake the driving forces. Analytical solutions reveal that the mechanism and process of acceleration and deceleration, and the halting are fundamentally different. This is indicated by the fact that the solutions to the accelerating system (1) appear in the form of the tangent hyperbolic functions with the upper or lower limits (depending on the initial condition), whereas the solutions for the decelerating system (2) appear to be in a special form of a decreasing tangent functions without bounds for which the lower bounds should be set practically, typically the velocity is zero as the mass halts.

5.1 Simple solutions

I begin analyzing the performances of the landslide models and their exact analytical solutions for the most simple situations where the motions can either be time-independent, or there is no internal deformation. Solutions will be presented and discussed for the decelerating motions, and the combination of accelerating and decelerating motions, and depositions.

5.1.1 Landslide deceleration

Landslide velocities in accelerating channels have been exclusively presented by Pudasaini and Krautblatter (2022). Here, I consider solutions in decelerating portion of the channel as well as the mass halting. It might be difficult to obtain initial velocity in the rapidly accelerating section in steep slope. But, in the lower portion of the track, where where motion switches from accelerating to decelerating state, one could relatively easily obtain the initial velocity that can be used further for dynamic computations. A simple situation arises when the landslide enters the transition zone, and to the fan region such that the initial velocity could be measured relatively easily at the fan mouth. Then, this information can be used to simulate the landslide velocity in the run-out zone, its travel time, and the run-out length in the fan area. Figure 1 shows results for decelerating motions. Once the landslide begins to decelerate (here, due to the negative net driving force), it decelerates faster in time than in space, means the (negative) time gradient of the velocity is higher than its (negative) spatial gradient. However, as it is closer to the deposition, the velocity decreases relatively smoothly in time. But, its spatial decrease is rather abrupt. The travel or run-out time and distance are determined by setting the deceleration velocity to zero in the solutions obtained for (4). We can consistently take initial time and location down the slope such that the previously accelerating mass now begins to decelerate. As the travel time and travel distance are directly connected by a function, we can uniquely determine the time and position at the instance the motion changes from accelerating to decelerating state. At this occasion, the solution switches from model (3) to model (4). In Fig. 1, I have suitably chosen the time and spatial boundaries (or initial conditions) as $x = 1500$ m corresponding to $t = 50$ s for $u_0 = 50$ ms^{-1}.

This analysis provides us with basic understanding of the decelerating motion and deposition process in the run-out region. I have analytically quantified the deceleration and deposition. The important observation from Fig. 1 is that the time and spatial perspectives of the landslide deceleration and deposition are fundamentally different. These are the manifestations of the inertial terms $\partial u/\partial t$ and $u\partial u/\partial x$ in the simple mass point and steady-state landslide velocity models (7) and (8), and (3) and (4), respectively.
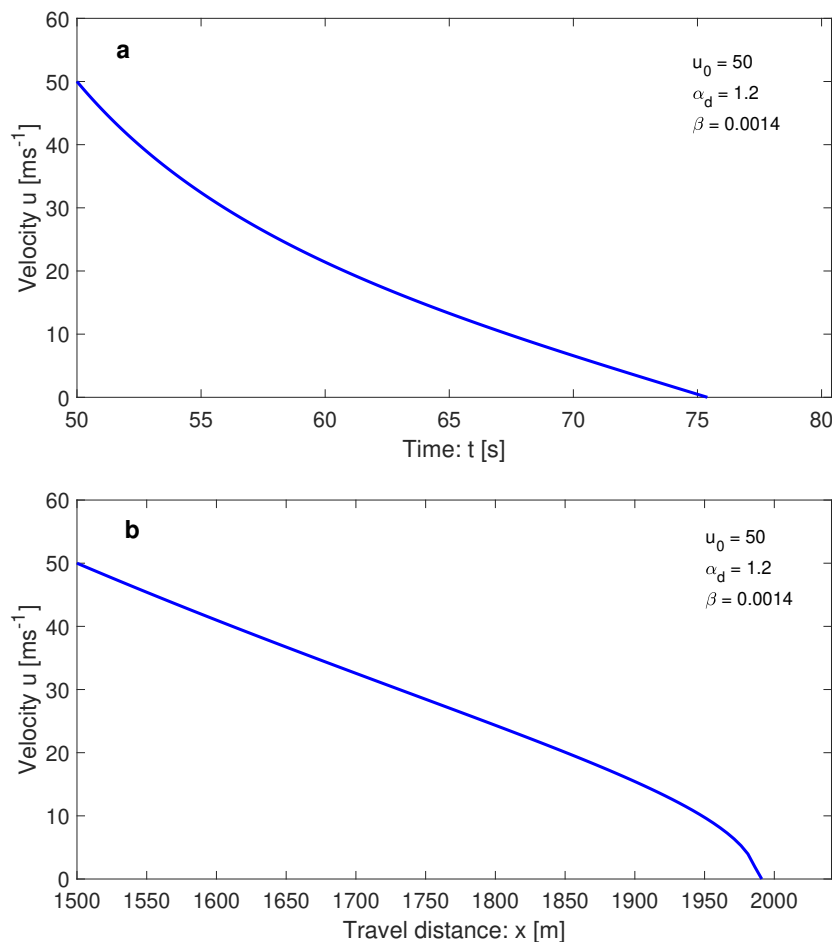
Figure 1: The landslide deceleration in time (**a**) and space (**b**) showing different dynamics for given physical parameters.

5.1.2 Landslide release and acceleration, deceleration and deposition: a transition

However, the above description is only one side of the total motion that must be unified with the solution in the accelerating sector, and continuously connect them to automatically generate the whole solution. For a rapid assessment of the landslide motion, technically the entire track can be divided into two major sectors, the ascending sector where the landslide accelerates, followed by the descending sector where it decelerates and finally comes to a halt. Assuming these approximations are practically admissible, this already drastically reduces the complexity and allows us to provide a quick solution. To achieve this, here, I combine both the solutions in the accelerating and decelerating portions of the channel. The process of landslide release and acceleration, and deceleration and deposition are presented in Fig. 2 in two segments (sectors), for ascending ($\alpha^a = 3.5$) and descending ($\alpha_d = 1.2$) sections, respectively. The initial value (left boundary) of the downstream decelerating segment is provided by the final value (right boundary) of the upstream accelerating segment. There are two key messages here. First, there are fundamental differences between the landslide release and acceleration, and deceleration and deposition in space and time. In space, the changes in velocity are rapid at the beginning of the mass release and acceleration and at the end of deceleration and deposition. However, in time, these processes (changes in velocity) are relatively gentle at the beginning of mass release and acceleration,
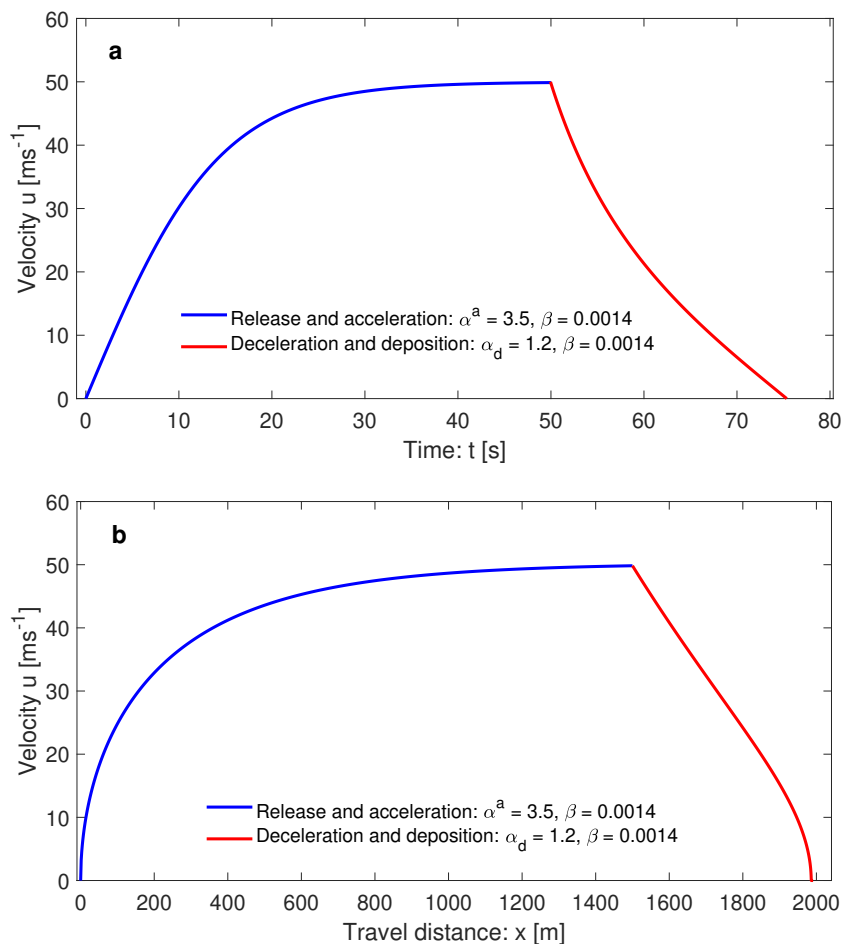
9

Figure 2: The landslide release and acceleration (left segments), deceleration and deposition (right segments) in time **(a)**, and space **(b)** with chosen physical parameters. Also seen is the transition from acceleration to deceleration at kinks at about (50, 50) and (1500, 50), respectively. The landslide velocity dynamics are fundamentally different in time and space.

and at the end of deceleration and deposition. This means, the spatial and time perspectives of changes of velocities are different. Second, the transition from acceleration to deceleration is of major interest, as this changes the state of motion from driving force dominance to resisting force dominance, here, due to the negative net driving force. The transition is more dramatic in time than in space. This manifests that the three critical regions; release, transition from acceleration to deceleration, and deposition; must be handled carefully as they provide very important information for the practitioners and hazard assessment professionals on the dynamics of landslide motion, behavioral changes in different states and depositions. This means, the initial velocity, the change in velocity from the accelerating to decelerating section, and the velocity close to the deposition must be understood and modelled properly.

5.1.3   Landslide release and acceleration, deceleration and deposition: multi-sectional transitions

The situations described above are only some rough approximations of reality as the landslide acceleration and deceleration may often change locally, requiring to break its analysis in multiple sectors to more realistically model the dynamics in greater details and higher accuracy to the observed data. In general, the landslide moves down a variable track. For practical purpose, such a track can be realistically divided in to a multi-sectional track (Dietrich and Krautblatter, 2019) such that at each section we can apply our analytical velocity solutions, both for accelerating (sufficiently positive net driving force in relation of the initial velocity, or the viscous drag force) and decelerating (negative net driving force) sections. The transitions between these sections automatically satisfy the boundary conditions: The left boundary (initial value) of the following segment is provided by the right boundary (final value) that is known from the analytical solution constructed in the previous time, or space of the preceding segment. This procedure continues as far as the two adjacent segments are joined, connecting either ascending−ascending, ascending−descending, or descending−descending velocity segments. However, note that, independent of the number of segments and their connections, only one initial (or boundary) value is required at the uppermost position of the channel. All other consecutive (internal and final) boundary conditions will be systematically generated by our analytical solution system, derived and explained at Section 3.

An ascending−ascending segment connection is formed when two ascending segments with different positive net driving forces (larger than the drag forces) are connected together. A typical example is the connection between a relatively slowly accelerating to a highly accelerating section. An ascending−descending segment connection is constituted when an upstream ascending segment is connected with a downstream descending segment, typically the connection between an accelerating to descending section. A descending−descending segment connection is developed when the two descending segments with different negative net driving forces are connected together. A typical example is the connection between a slowly decelerating to a highly decelerating section. However, many other combinations between ascending and descending segments can be formed as guided by the changes in the net driving forces, or the changes in the slope-induced and friction-induced forces and their dominances. So, we need to extend the solution procedure of Section 5.1.2 from two sectoral landslide transition to multi-sectoral transitions.

Figure 3 presents a typical (positive rate of ascendant, and negative rate of descendant) example of the multi-sectoral solutions for the time evolution of the velocity field for the ascending ($\alpha^a = 4.0, 5.0, 6.0$), and the descending ($\alpha_d = 0.15, 1.25, 1.90$) sectors, respectively. However, note that the α values on the ascending and descending sectors are relative to each other. So, α_d on the descending sectors should be perceived as relatively negative to α^a in the ascending sector. In the ascending sectors, as the net driving force increases, from the first to the second to the third sector, the mass further accelerates, enhancing the slope of the velocity field at each successive kink connecting the two neighboring segments. At the major kink, as the net driving force changes rapidly from accelerating to decelerating mode with the value of $\alpha^a = 6.0$ to $\alpha_d = 0.15$, the motion switches dramatically from the velocity ascending to descending state. In the following descending sectors, as the values of α_d quickly increases, the mass further decelerates, from the fourth to the fifth to the sixth sector, negatively reducing the slope of the velocity field at each successive kink, preparing for deposition. Finally, the mass comes to a halt ($u = 0$) at $t = 50$ s. So, Fig. 3 reveals important time dynamics of ever-increasing multi-sectoral ascending motions, its quick transition to descending motion, and the following ever-decreasing descending motions, and the final mass halting. The main observation is the analytical quantification of the complex dynamics of the landslide with increasing and decreasing gradients of the positive and negative net driving forces. This can be a scenario for a track with multi-sectors of ever increasing slope, followed by a quick transition to a decreasing slope, again succeeded by multi-sectors of ever decreasing slopes, and finally mass deposition.

As the time and spatial perspectives of the landslide motions are different, and from the practical point of view, it is even more important to acquire the velocity as a function of the channel position, next, I present results for multi-sectoral landslide dynamics as a function of the channel position. Depending on the rates of ascendance and descendance, I analyze the landslide dynamics separately. Figure 4 displays the results for the
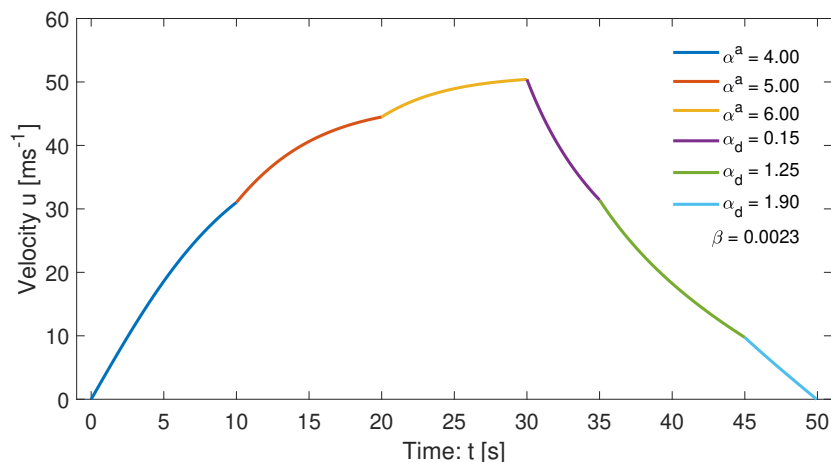
Figure 3: Landslide release and multi-sectional acceleration, deceleration and deposition in time. The physical parameters are shown in the legend. Several ascending−ascending and descending−descending segments are connected on the left with kinks at $(10, 31.02)$ and $(20, 44.48)$, and on the right with kinks at $(35, 31.40)$ and $(45, 9.75)$. The left and right segments are further connected by a central ascending−descending segment connection at the major kink at $(30, 50.41)$. The mass stops at $(50, 0.0)$.

377 evolution of the velocity field as a function of the travel distance as the landslide moves down the slope. To
378 investigate the influence of the intensity of accelerating and decelerating net driving forces, two distinct sets
379 of net driving forces are considered. In Fig. 4a, as the net driving force increases from the first to second
380 to the third sectors, the acceleration increases, and the slopes of the velocity curves increase accordingly at
381 kinks in these sectors. But, as the net driving force decreases from the third to fourth to the fifth sectors, the
382 acceleration decreases although the landmass is still accelerating. In this situation, the velocity curves increase
383 accordingly in these sectors, but slowly, and finally reach the maximum value. At the major kink, the net
384 driving force has dropped quickly from $\alpha^a = 3.06$ to its decelerating value of $\alpha_d = 0.5$. Consequently, the
385 motion switches dramatically from the velocity ascending (accelerating) to descending (decelerating) state. In
386 the velocity descending sectors, as the values of α_d quickly increases, the mass further decelerates, but now
387 much quicker than before, resulting in the negatively increased slope of the velocity fields at each successive
388 kink. As controlled by the net decelerating force, α_d, the deposition process turned out to be rapid. Finally,
389 the mass comes to a halt ($u = 0$) at $x = 1494$ m.

390 In Fig. 4b, the net driving driving force in the first sector is much higher than that in Fig. 4a. However,
391 then, even in the ascending sectors, the net driving forces are steadily decreasing, resulting in the continuously
392 decreased slopes of the velocity fields from the first to the fifth sectors. As in Fig. 4a, at the major kink, the
393 net driving force dropped quickly from $\alpha^a = 3.79$ to its decelerating value of $\alpha_d = 0.5$, forcing the motion to
394 switch dramatically from the velocity ascending to descending state. In the velocity descending sectors, as the
395 values of α_d further increases, the mass decelerates steadily, faster than before, with the negatively increased
396 slope of the velocity fields at each following kink. Due to the similar decelerating net driving forces as in Fig.
397 4a, the deposition process turned out to be quite quick. Finally, the mass halts ($u = 0$) at $x = 1435$ m, a bit
398 earlier than in Fig. 4a. So, Fig. 4 manifests that the slopes and connection appearances of the velocity fields
399 exclusively depend on the boundary values and the net driving forces of the following sections.

400 The run-out distances in Fig. 4a and Fig 4b are similar. However, their internal dynamics are substantially
401 different, here, mainly in the ascending sectors. The main essence here is that one cannot understand the
402 overall dynamics of the landslide by just looking at the final deposit and the run-out length as in empirical and
403 statistical models. Instead, one must also understand the entire and the internal dynamics in order to properly
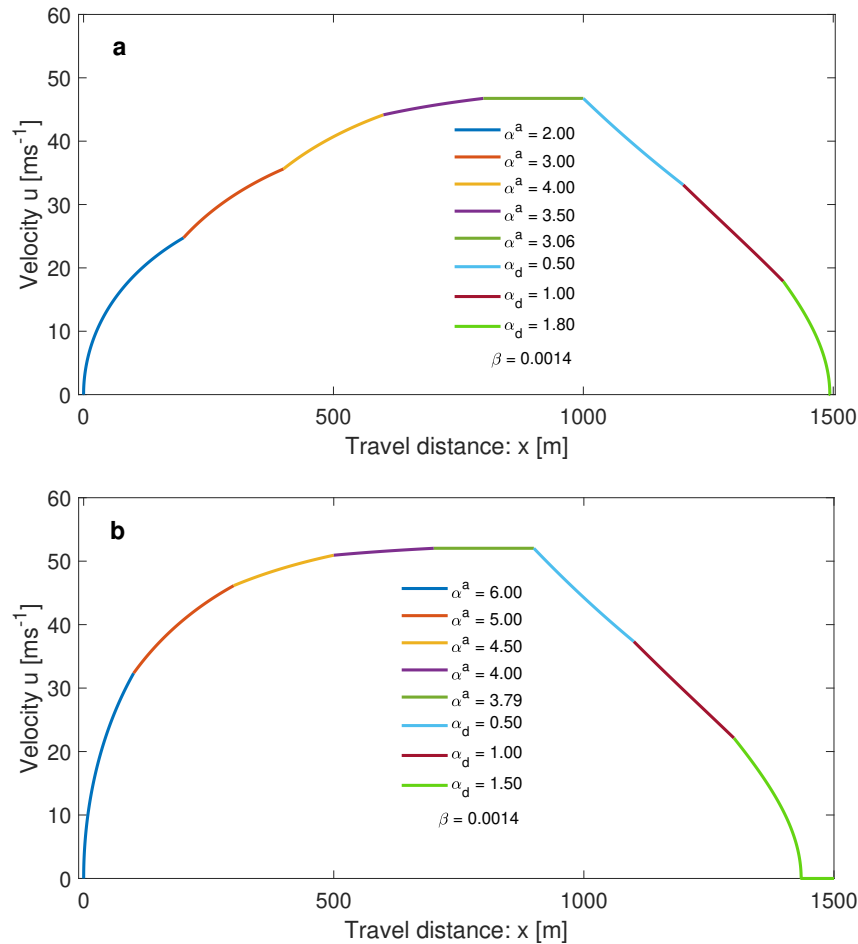
Figure 4: Landslide release and multi-sectional acceleration, deceleration and deposition in space with different parameter sets shown in the legends. **(a)** Several ascending−ascending segments are connected on the left with kinks at (200, 24.75), (400, 35.62), (600, 44.20), and (800, 46.75), and descending−descending segments are connected on right with kinks at (1200, 33.10), and (1400, 17.90). The left and right segments are further connected by a central ascending−descending segment connection at the major kink at (1000, 46.80). The landslide comes to a halt at (1494, 0.0). **(b)** Similarly, several ascending−ascending segments are connected on the left with kinks at (100, 32.35), (300, 46.14), (500, 50.94), and (700, 52.03), and descending−descending segments are connected on the right with kinks at (1100, 37.30), and (1300, 22.10). The left and right segments are further connected by a central ascending−descending segment connection at the major kink at (900, 52.03). The landslide comes to a halt at (1435, 0.0). Although **(a)** and **(b)** have similar run-out distances, their internal dynamics are different, so are the associated impact forces along the tracks.

404   simulate the motion and the associated impact force. So, our physics-based complete analytical solutions
405   provide much better descriptions of landslide dynamics than the angle of reach based empirical or statistical
406   models (Heim, 1932; Lied and Bakkehøi, 1980) that explicitly rely on parameter fits (Pudasaini and Hutter,
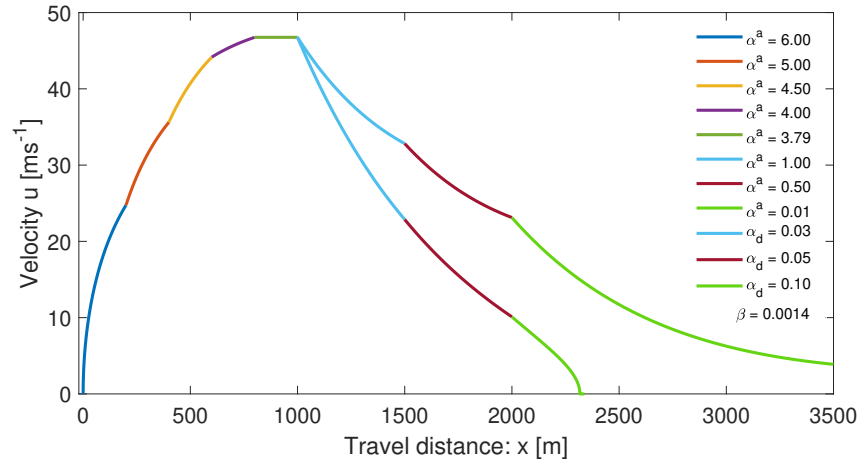407   2007).

Figure 5: Landslide release and multi-sectional acceleration, deceleration and deposition in space with different physical parameters sets shown in the legend. Two different decelerating motions are considered for the right sectors. The upper velocities on the right are produced with the solution of the model (1) with positive net driving forces producing kinks at (1500, 32.82) and (2000, 23.12), whereas the lower velocities on the right are produced with the solution of the model (2) with negative net driving forces producing kinks as (1500, 22.87) and (2000, 10.10), respectively. The corresponding descending motions in the common track domains are displayed with the same color-codes. Their dynamics and deposition processes are quite different. The negative net driving forces result in the realistic deceleration, run-out and deposition at (2317, 0), while even after travelling 3500 m, the decelerating motion with positive net driving forces still has high velocity (3.88 ms^{-1}), and cannot represent reality.

5.1.4 Decelerating landslide with positive and negative net driving forces

The previously accelerating landslide may transit to decelerating motion such that the net driving force α^a is positive in both sections, but α^a is smaller in the succeeding section, i.e., $\alpha_p^a > \alpha_s^a$, where, $_p$ and $_s$ indicate the preceding and succeeding sections. Assume that the end velocity of the preceding section is u_p. Then, if $u_p > \sqrt{\alpha_s^a/\beta}$, the landslide will decelerate in the succeeding section such that the velocity in this section is bounded from below by $\sqrt{\alpha_s^a/\beta}$. This can happen when the slope decreases and/or friction increases, but, still, the net driving force remains positive. However, as the initial velocity of the succeeding section is higher than the characteristic limit velocity of this section, $\sqrt{\alpha_s^a/\beta}$, the velocity must decrease as it is controlled by the resisting force, namely the drag. If the slope is quite long with this state, the landslide velocity will approach $\sqrt{\alpha_s^a/\beta}$, and then, continue almost unchanged. A particular situation is the vanishing net driving force, i.e., $\alpha_s^a = 0$, in the right section. This can prevail when the gravity and frictional forces balance each other. Then, as the landslide started with the positive (high) velocity in the left boundary of the right section, it is continuously resisted by the drag force, strongly at the beginning, and slowly afterwards, as the velocity decreases substantially. If the channel is sufficiently long (and $\alpha_s^a = 0$), then the drag can ultimately bring the landslide velocity down to zero. Yet, this is a less likely scenario to take place in nature. In all these situations, which are associated with the positive net driving forces, we must consistently use the model (1) and its corresponding analytical solutions. In another scenario, assume that the landslide transits to the next section where it experiences the negative net driving force. Then, in this section, we must use the model (2) and its corresponding analytical solutions.

Figure 5 presents the first rapidly accelerating motions in the left sections, as in Fig. 4a, followed by decelerating motions in the right sections. However, as the mass transits to the right sections at $x = 1000$, there can be fundamentally two types of decelerating motions. (i) The motions can still be associated with the positive net

430 driving forces. Or, (ii) the motions must be associated with the negative net driving forces. This depends
431 on the actual physical situation, and either (i) or (ii) can be true. The lower velocities on the right are
432 produced with the solution of the model (2) with negative net driving forces, whereas the upper velocities
433 are produced with the solution of the model (1) with positive net driving forces. For better visualization,
434 and ease of comparison, the domain of decelerating motion and deposition has been substantially enlarged.
435 The important point is that, the two solutions on the right show completely different dynamics. On the one
436 hand, the decelerating solutions represented by the upper curves on the right are less realistic as these take
437 unrealistically long time until the mass comes to stop, and the velocities are also unreasonably high. On the
438 other hand, such solutions can mainly be applied for the relatively low positive net driving forces and high
439 initial velocities. However, the lower curves on the right are realistic, and are produced by using the solutions
440 for the naturally decelerating motions associated with the negative net driving forces, as is the case in natural
441 setting. For the solutions described by the negative net driving forces, the mass deceleration is fast, velocity
442 is low, close to the flow halting the velocity drops quickly to zero, and the landslide stops realistically as
443 expected. Figure 5 is of practical importance as it clearly reveals the fact that we must appropriately model
444 the descending landslide motions. The important message here is that the descending and deposition processes
445 of a landslide must be described by the decelerating solutions with negative net driving forces (the solutions
446 derived here), but not with the decelerating solutions described by positive net driving forces (the solutions
447 derived in Pudasaini and Krautblatter, 2022). So, Fig. 5 has strong implications in real applications that the
448 new set of analytical solutions with negative net driving forces must be appropriately considered in describing
449 the descending landslide motion.

5.2 Time and spatial evolution of landslide velocity: general solutions

451 The solutions presented in Section 5.1 only provide information of the landslide dynamics either in time or in
452 space, but not the both. As the landslide moves down the slope, in general, its velocity evolves as a function of
453 time and space. Pudasaini and Krautblatter (2022) presented the time marching of the landslide motion that
454 also stretches as it accelerates downslope. Such deformation of the landslide stems from the advection, $u\partial u/\partial x$,
455 and the applied forces, $\alpha^a - \beta u^2$. The mechanism of landslide advection, stretching and the velocity up-lifting
456 has been explained. They revealed the fact that shifting, up-lifting and stretching of the velocity field emanate
457 from the forcing and non-linear advection. The intrinsic mechanism of their solution describes the breaking
458 wave and emergence of landslide folding. This happens collectively as the solution system simultaneously
459 introduces downslope propagation of the domain, velocity up-lift and non-linear advection. Pudasaini and
460 Krautblatter (2022) disclosed that the domain translation and stretching solely depends on the net driving
461 force, and along with advection, the viscous drag fully controls the shock wave generation, wave breaking,
462 folding, and also the velocity magnitude.

463 Pudasaini and Krautblatter (2022) considered the accelerating motion. Assuming that the landslide has already
464 propagated a sufficient distance downslope, here, I focus on time and spatial evolution of landslide velocity for
465 the decelerating motion and deposition for which I apply the new solutions given by (21)-(22). This complements
466 the existing solutions and presents the unified analytical description of the landslide motion down the entire
467 slope. So, next I present more general results for landslide velocity for decelerating motion controlled by the
468 advection, $u\partial u/\partial x$, and the applied forces, $-\alpha_d - \beta u^2$. In contrast to the accelerating motion, the decelerating
469 motion is associated with the applied force $-\alpha_d - \beta u^2$, while the structure of the advection, $u\partial u/\partial x$, remains
470 unchanged. Now, the landslide may be stretched or compressed, however, the velocity will gradually sink. The
471 intensity of the wave breaking and the landslide folding will be reduced. This happens, because the solution
472 system introduces downslope propagation of the domain, velocity sink and non-linear advection. Moreover, the
473 domain translation and stretching or contracting depends on the net driving force, and paired with advection,
474 the viscous drag controls the shock wave generation, wave breaking, folding, and also the reduction of the
475 velocity magnitude.

476 From the geomorphological, engineering, planning and hazard mitigation point of view, the deposition and run-
477 out processes are probably the most important aspects of the landslide dynamics. So, in this section, I focus
478 on the dynamics of the landslide as it decelerates and enters the run-out area and the process of deposition,
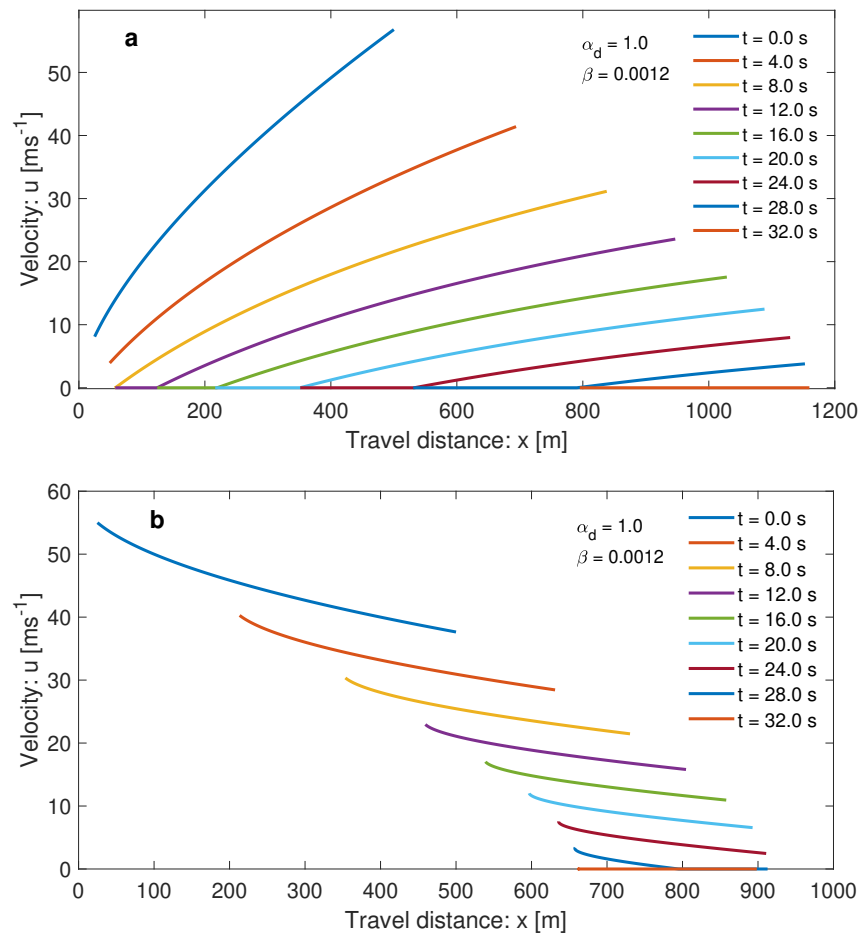
Figure 6: Time and spatial evolution of the landslide velocity showing the motion, deformation and deposition of initially ascending **(a)**, and descending **(b)** landslide fronts, described by $s_0(x) = x^{0.65}$ and $s_0(x) = 60 - x^{0.5}$, respectively, at $t = 0$ s. The physical parameter values are shown. The initially different velocity profiles result in completely different travel distances and landslide spreadings or contractings. The deposition extend for the ascending front is much longer than the same for the descending front.

479 including its stretching or contracting behavior.

480 **5.2.1 Landslide depositions of initially ascending and descending fronts**

481 In the most simple situation, the landslide may start deceleration and enter the run-out and the fan zone
482 with either the ascending or descending front. An ascending front may represent the pre-mature transition,
483 while a descending front may signal the mature transition to the run-out zone. Figure 6 describes the prop-
484 agation dynamics and deposition processes for initially ascending (a) and descending (b) fronts. The initial
485 velocity distributions are chosen following Pudasaini and Krautblatter (2022). In Fig. 6a, the front decelerates
486 much faster than the rear, while in Fig. 6b, it is the opposite. This leads to the forward propagating and
487 elongating landslide mass for the ascending front while forward propagating and compressing landslide mass
488 for the descending front. This results in completely different travel distances and deposition processes. The
489 runout distance is much longer in Fig. 6a than in Fig. 6b. The striking difference is observed in the lengths
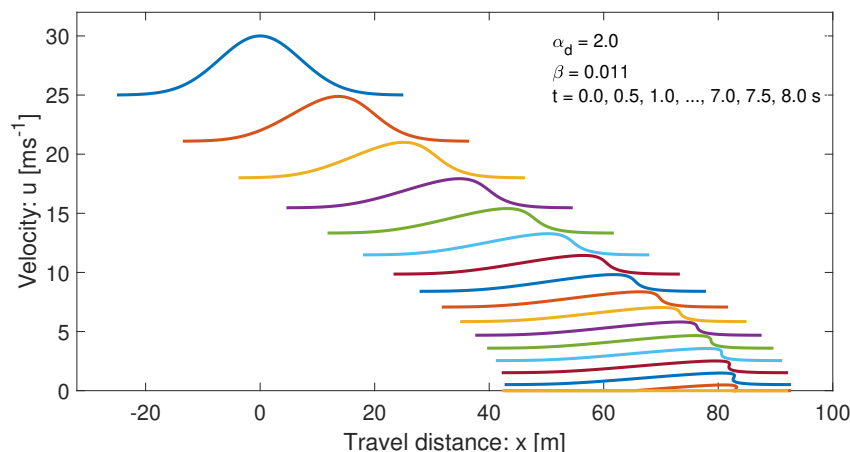
16

Figure 7: Time and space evolution of the propagating landslide and deposition waves. The initial velocity distribution is given by $s_0(x) = 5 \exp\left[-x^2/100\right] + 25$ at $t = 0$ s. The physical parameter values are shown.

of the deposited masses. The deposition extend for the ascending front is much longer (about 1100 m) than the same for the descending front (which is < 250 m). At a first glance, it is astonishing. However, it can be explained mechanically. Ascending or descending fronts lead to the strongly stretching and compressing behavior, resulting, respectively, in the very elongated and compressed depositions of the landslide masses. In Fig. 6a, although the front decelerates faster than the rear, the rear velocity drops to zero faster than the front, whereas the velocity of the front becomes zero at a later time. So, the halting process begins much earlier, first from the rear and propagates to the front that takes quite a while. This results in the remarkable stretching of the landslide. Nevertheless, in Fig. 6b, although the rear decelerates faster than the front, the front velocity quickly drops to zero much faster than the rear, whereas the velocity of the rear becomes zero at a much later time. So, the halting process begins first from the front and propagates to the rear that takes quite a while. This results in the remarkable compression of the landslide. This demonstrates how the different initial velocity profiles of the landslides result in completely different travel distances and spreadings or contractings in depositions.

The state of deposition is important in properly understanding the at-rest-structure of the landmass for geomorphological and civil or environmental engineering considerations. Energy dissipation structures, e.g., breaking mounds, can be installed in the transition and the run-out zones to substantially reduce the landslide velocity (Pudasaini and Hutter, 2007; Johannesson et al., 2009). Here comes the direct application of our analytical solution method. The important message here is that, if we can control the ascending frontal velocity of the landslide and turn it into a descending front, by some means of the structural measure in the transition or the run-out zone, we might increase compaction and control the run-out length. This will have a immediate and great engineering and planning implications, due to increased compaction of the deposited material and the largely controlled travel distance and deposition length.

5.2.2 Landslide deposition waves

The situation discussed in the preceding section only considers a monotonically increasing or a monotonically decreasing velocity front in the transition or run-out (fan) zones. However, in reality, the landslide may enter transition or the fan zone with a complex wave form, representative of a surge wave. A more general situation is depicted in Fig. 7 which continuously combines the ascending and descending parts in Fig. 6, but also includes upstream and downstream constant portions of the landslide velocities thus, forming a wave structure. The initial velocity distribution is chosen following Pudasaini and Krautblatter (2022). As the frontal and
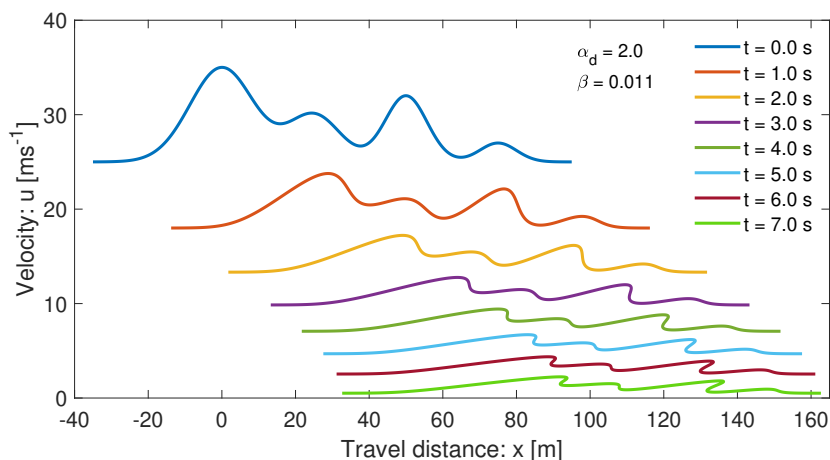
Figure 8: Time and space evolution of the landslide with multiple complex waves, foldings and crests during the propagation and deposition processes. The initial velocity distribution ($t = 0$ s) is given by the function $s_0(x) = 10 \exp\left[-(x-0)^2/150\right] + 5\exp\left[-(x-25)^2/100\right] + 7\exp\left[-(x-50)^2/65\right] + 2\exp\left[-(x-75)^2/50\right] + 25$. The chosen physical parameter values are shown in the legend.

519 the rear portions of the landslide initially have constant velocities, due to its initial velocity distribution with
520 maximum in between, it produces a pleasing propagation mosaic and the final settlement. Because, now, both
521 the front and the rear decelerate at the same rates, deposition begins from both sides. Although, in total, the
522 landslide elongates (but not that much), it mainly elongates in the rear side while compressing a bit in the
523 frontal portion. The velocity becomes smoother in the back side of the main peak while it tends to produce a
524 kink in the frontal region. This forces to generate a folding in the frontal part which is seen closer to the halting.
525 However, the folding is controlled by the relatively high applied drag. If the applied drag would have been
526 substantially reduced, dominant folding would have been observed. Note that, the folding of the accelerating
527 landslide has been covered in Pudasaini and Krautblatter (2022). The important idea here is that, the folding
528 and the wave that may be present in the frontal part of the landslide evolution or deposition, can be quantified
529 and described by our general exact analytical solution.

5.2.3 Landslide with multiple waves, foldings, crests and deposition pattern

531 The landslide may descend down and enter the transition and the run-out zone with multiple surges of different
532 strengths, as frequently observed in natural events. In reality, the initial velocity can be even more complex
533 than the one utilized in Fig. 7. To describe such situation, Fig. 8 considers a more general initial velocity
534 distribution than before with multiple peaks and troughs of different strengths and extents represented by a
535 complex function. As the landslide moves down, it produces a beautiful propagation pattern with different
536 stretchings and contractings resulting in multiple waves, foldings, crests and deposition. Depending on the
537 initial local velocity distribution (on the left and right side of the peak), in some regions, strong foldings and
538 crests are developed (corresponding to the first and third initial peaks), while in other regions only weak folding
539 (corresponding to the second initial peak) is developed, or even the peak is diffused (corresponding to the fourth
540 initial peak). This provides us with the possibility of analytically describing complex multiple waves, foldings
541 and crests formations during the landslide motion and also in deposition. This analysis can provide us with
542 crucial information of a complex deposition pattern that can be essential for the study of the geomorphology
543 of deposit. Importantly, the local information of the degree of compaction and folding can play a vital role in
544 landuse planning, and decision making, e.g., for the choice of the location for the infrastructural development.

545 Technically, the results presented in Fig. 2 to Fig. 8 demonstrate that, computationally costly simulations may

now be replaced by a simple highly cost-effective, clean and honourable analytical solutions (almost without any cost). This is a great advantage as it provides immediate and very easy solution to the complex landslide motion once we know the track geometry and the material parameters, which, in general, is known from the field. So, we have presented a seminal technique describing the entire landslide motion and deposition process.

6 Summary

I have constructed several new exact analytical solutions and combined these with the existing solutions for the landslide velocity. This facilitated the unified description of a landslide down a slope with multiple segments with accelerating and decelerating movements as well as the landslide run-out, and deposition. This provided the complete and righteous depiction of the landslide motions in different segments, for the entire slope, from its release, through the track until it comes to a standstill. Our analytical method couples several ascending−ascending, ascending−descending, or descending−descending segments to construct the exact multi-sectoral velocity solutions down the entire track. I have analytically quantified the complicated landslide dynamics with increasing and decreasing gradients of the positive and negative net driving forces. The implication is: the new set of analytical solutions with negative net driving forces must be appropriately considered in real applications in describing the descending landslide motion as such solutions better represent the natural process of decreasing motion and deposition. Analytical solutions revealed essentially different novel mechanisms and processes of acceleration and deceleration and the mass halting. There are fundamental differences between the landslide release and acceleration, and deceleration and deposition in space and time. The transition from acceleration to deceleration takes place with strong kinks that changes the state of motion from a primarily driving force dominance to resisting force dominance region. This manifests the three critical regions; release, transition from acceleration to deceleration, and deposition; that must be handled carefully. The time and spatial perspectives of the landslide deceleration and deposition appeared to be fundamentally different as the transition is more dramatic in time than in space. We can uniquely ascertain the exact time and position at the instance the motion changes from accelerating to decelerating state. Considering all the ascending and descending motions, we can analytically obtain the exact total travel time and the travel distance for the whole motion. These quantities are of direct practical importance as they supply us with all the necessary information to fully describe the landslide dynamics.

Our physics-based complete, general analytical solutions disclose a number of important information for the practitioners and hazard assessment professionals on the vitally important physics of landslide motion and settlement. Essentially, these solutions provide much better overall descriptions of landslide dynamics than the empirical or statistical models, which explicitly rely on parameter fits, but can only deal with the run-out length. Our models provide information on the entire and internal dynamics that is needed to properly simulate the motion and associated impact force. Our solutions provide insights into the process of compaction, and the mechanism to control the travel distance and deposition length. The frontal folding and the wave, that may appear during the landslide evolution or deposition, can be quantified by our analytical solution. We have demonstrated that different initial landslide velocity distributions result in completely dissimilar travel distances, deposition processes, and spreadings or contractings. Ascending and descending fronts lead to the strongly stretching and compressing behavior resulting, respectively, in the very elongated and shortened run-outs. The striking difference is observed in the lengths of the deposited masses. Time and space evolution of the marching landslide and deposition waves produce a beautiful pattern and the final settlement. Initial velocity distribution with multiple peaks and troughs of different strengths and extents lead to a spectacular propagation pattern with distinct stretchings and contractings resulting in multiple waves, foldings, crests and depositions. Depending on the initial local velocity distribution, in some regions strong foldings and crests are developed, while in other regions foldings and crests are diffused. This provides us with the possibility of analytically describing complex multiple waves, foldings and crests formations during the landslide motion and deposition. As complex multiple surges of varying strengths can be explained analytically, our method provides us with crucial geomorphological information of the sophisticated deposition pattern, including the important local state of compaction and folding, which play a vital role in landuse planning, and decision making for the infrastructural development and environmental protection. Moreover, our analytical method demonstrates

Earth Surface
Dynamics
Discussions

that computationally costly solutions may now be replaced by a simple, highly cost-effective and unified ana-
lytical solutions (almost without any cost) down the entire track of the landslide. This is of a great technical
advantage for the landslide practitioners and engineers as it provides immediate and very easy solution to the
complex landslide motion.

Acknowledgements

References

[1] Baselt, I., de Oliveira, G.Q., Fischer, J.-T., Pudasaini, S.P., 2021. Evolution of stony debris flows in laboratory experiments. Geomorphology 372, 107431. https://doi.org/10.1016/j.geomorph.2020.107431.

[2] Berger, C., McArdell, B.W., Schlunegger, F., 2011. Direct measurement of channel erosion by debris flows, Illgraben, Switzerland. J. Geophys. Res. Earth Surf. 116, F01002.

[3] Burgers, J.M., 1948. A mathematical model illustrating the theory of turbulence. In Advances in Applied Mechanics, pp 171-199. Academic Press Inc., New York, edited by Richard von Mises and Theodore von Karman.

[4] Chalfen, M., Niemiec, A., 1986. Analytical and numerical solution of Saint-Venant equations. Journal of Hydrology 86(1-2), 1-13.

[5] Cuomo, S., Pastor, M., Capobianco, V., Cascini, L., 2016. Modelling the space time evolution of bed entrainment for flow-like landslides. Engineering Geology 212, 10-20.

[6] de Haas, T., Nijland, W., de Jong, S.M., McArdell, B.W., 2020. How memory effects, check dams, and channel geometry control erosion and deposition by debris flows. Scientific Reports. 10, 14024. https://doi.org/10.1038/s41598-020-71016-8.

[7] de Haas, T., van Woerkom, T., 2016. Bed scour by debris flows: experimental investigation of effects of debris flow composition. Earth Surf. Process. Landforms 41, 1951-1966.

[8] Dietrich, A., Krautblatter, M., 2019. Deciphering controls for debris-flow erosion derived from a liDAR-recorded extreme event and a calibrated numerical model (Rossbichelbach, Germany). Earth Surf. Process. Landform 44, 1346-1361.

[9] Dowling, C.A., Santi, P.M., 2014. Debris flows and their toll on human life: a global analysis of debris-flow fatalities from 1950 to 2011. Nat. Hazards 71(1), 203-227.

[10] Evans, S.G., Bishop, N.F., Smoll, L.F., Murillo, P.V., Delaney, K.B., Oliver-Smith, A., 2009. A re-examination of the mechanism and human impact of catastrophic mass flows originating on Nevado Huascaran, Cordillera Blanca, Peru in 1962 and 1970. Eng. Geol. 108, 96-118

[11] Faraoni, V., 2022. Helmoltz problem for the Riccati equation from an analogous Friedmann equation. Eur. Phys. J. C 82. https://doi.org/10.1140/eplc/s10052-021-09966-0.

[12] Faug, T., Chanut, B., Beguin, R., Naaim, M., Thibert, E., Baraudi, D., 2010. A simple analytical model for pressure on obstacles induced by snow avalanches. Ann. Glaciol. 51 (54), 1-8.

[13] Frank, F., McArdell, B.W., Huggel, C., Vieli, A., 2015. The importance of entrainment and bulking on debris flow runout modeling: examples from the Swiss Alps. Nat. Hazards Earth Syst. Sci. 15, 2569-2583.

[14] Gauer, P., 2018. Considerations on scaling behavior in avalanche flow along cycloidal and parabolic tracks. Cold Reg. Sci. Technol. 151, 34-36.

[15] Gubler, H., 1989. Comparison of three models of avalanche dynamics. Annals of Glaciology 13, 82-89.

[16] Heim, A., 1932. Bergsturz und menschenleben. Geologische Nachlese Nr. 30, Naturforschenden Gesellschaft in Zürich 77, 220.

[17] Iverson, R. M., Ouyang, C., 2015. Entrainment of bed material by earth-surface mass flows: review and reformulation of depth-integrated theory. Rev. Geophys. 53(1), 27-58.

[18] Johannesson, T., Gauer, P., Issler, D., Lied, K., 2009. In: Barbolini, M., Domaas, U., Harbitz, C.B., Johannesson, T., Gauer, P., Issler, D., Lied, K., Faug, T., Naaim, M. (Eds.), The Design of Avalanche Protection Dams. Recent Practical and Theoretical Developments. European Commision. Directorate General for Research.

[19] Le, L., Pitman, E.B., 2009. A model for granular flows over an erodible surface. SIAM J. Appl. Math. 70, 1407-1427.

[20] Lied, K., Bakkehøi, S. 1980. Empirical calculations of snow-avalanche run-out distance based on topographic parameters. Journal of Glaciology V26, 165–178.

[21] Liu, W., Yang, Z., He, S., 2021. Modeling the landslide-generated debris flow from formation to propagation and run-out by considering the effect of vegetation. Landslides 18, 43–58.

[22] McClung, D.M., 1983. Derivation of Voellmy's Maximum Speed and Run-Out Estimates from a Centre-of-Mass Model. Journal of Glaciology 29(102), 350-352.

[23] McDougall, S., Hungr, O., 2005. Dynamic modelling of entrainment in rapid landslides. Can. Geotech. J. 42, 1437-1448.

[24] Mergili, M., Jaboyedoff, M., Pullarello, J., Pudasaini, S.P., 2020. Back calculation of the 2017 Piz Cengalo - Bondo landslide cascade with r.avaflow: what we can do and what we can learn. Nat. Hazards Earth Syst. Sci. 20, 505-520.

[25] Montecinos, G.I., 2015. Analytic solutions for the Burgers equation with source terms. arXiv:1503.09079v1.

[26] Perla, R., Cheng, T.T., McClung, D.M., 1980. A two-parameter model for snow-avalanche motion. J. Glaciology 26(94), 197-207.

[27] Pilvar, M., Pouraghniaei, M.J., Shakibaeinia, A., 2019. Two-dimensional sub-aerial, submerged, and transitional granular slides. Physics of Fluids 31, 113303. https://doi.org/10.1063/1.5121881.

[28] Pudasaini, S.P., Krautblatter, M., 2022. The landslide velocity. Earth Surf. Dynam. 10, 165–189, https://doi.org/10.5194/esurf-10-165-2022, 2022.

[29] Pudasaini, S.P., Krautblatter, M., 2021. The mechanics of landslide mobility with erosion. Nat. Commun. 12, 6793, https://doi.org/10.1038/s41467-021-26959-5, 2021.

[30] Pudasaini, S.P., Mergili, M., 2019. A multi-phase mass flow model. Journal of Geophysical Research: Earth Surface, 124, 2920-2942.

[31] Pudasaini, S.P., 2016. A novel description of fluid flow in porous and debris materials. Eng. Geol. 202, 62-73.

[32] Pudasaini, S.P., 2012. A general two-phase debris flow model. J. Geophysics. Res. 117, F03010. doi:10.1029/2011JF002186.

[33] Pudasaini, S.P., Hutter, K., 2007. Avalanche Dynamics: Dynamics of Rapid Flows of Dense Granular Avalanches. Springer, Berlin, New York.

[34] Salm, B., 1966. Contribution to avalanche dynamics. International Symposium on Scientific Aspects of Snow and Ice Avalanches, 1965, Davos; pp. 199-214: IAHS Publ. No. 69.

[35] Shugar, D. H., Jacquemart, M., Shean, D., et al., 2021. A massive rockand ice avalanche caused the 2021 disaster at Chamoli, Indian Himalaya. Science 373, 300–306.

[36] Theule, J.I., Liebault, F., Laigle, D., Loye, A., Jaboyedoff, M., 2015. Channel scour and fill by debris flows and bedload transport. Geomorphology 243, 92-105.

[37] Voellmy. A., 1955. Über die Zerstörungskraft von Lawinen. Schweizerische Bauzeitung. Jahrg. 73. Ht. 12., 159-162; Ht. 15, 212-217; Ht. 17, 246-249: Ht. 19, 280-285. On the destructive force of avalanches, Translation No. 2. Alta. Avalanche Study Center, USDA, Forest Service, 1964.